Light-driven electron transfer by Quantum vibronic ratcheting

Partha Pratim Roy[1,2], Zachary X. W. Widel[3], Rui Liu[3], Jesús Valdiviezo[1,3,4,8], Peng Zhang[3], Cristina Leonardo[1,2], Jarrett P. Mansergh[3], Sutirtha Chowdhury[3], David N. Beratan[3,5,6], Michael J. Therien[3] and Graham R. Fleming[1,2,7]*

Affiliations:

[1]Department of Chemistry, University of California, Berkeley, CA 94720, USA.

[2]Molecular Biophysics and Integrated Bioimaging Division, Lawrence Berkeley National Laboratory, Berkeley, CA 94720, USA.

[3]Department of Chemistry, Duke University, Durham, North Carolina 27708, United States.

[4]Department of Electrical and Computer Engineering, Duke University, Durham, North Carolina 27708, United States.

[5]Department of Physics, Duke University, Durham, North Carolina 27708, United States.

[6]Department of Biochemistry, Duke University, Durham, North Carolina 27710, United States.

[7]Kavli Energy Nanoscience Institute at Berkeley, Berkeley, CA 94720, USA.

[8]Kenneth S. Pitzer Center for Theoretical Chemistry, Berkeley, CA 94720, USA.

*Corresponding author. Email: grfleming@lbl.gov

Abstract: The optical control of coherence to improve and create a new molecular function is a grand challenge in science. In this work, we present a synthetic strategy to build a donor-donor-acceptor (D_1D_2A) supramolecular construct and tailor vibronic coherence to leverage an efficient long-range electron-transfer by defeating the thermodynamic energy trap imposed by Boltzmann statistics. The relaxed D_1* lies 0.35 eV below the D_2* state. By a combined transient IR and two-dimensional electronic vibrational spectroscopy study we show that selective excitation of the vibronic bands of lower energy primary donor (D_1) leads to substantial rapid (<200 fs) formation of a charge-transfer state ($D_1D_2^+A^-$), followed by hole transfer leading to ($D_1^+D_2A^-$). This provides direct evidence of electron transfer (secondary donor D_2 to A) induced by a vibronic quantum ratcheted 'uphill' energy transfer from D_1 to D_2. Thus, it lays out a rational for improving efficiency of solar energy conversion and expanding the spectral bandwidth in synthetic light harvesting systems.

One-Sentence Summary: A molecular quantum energy ratchet is engineered to leverage an efficient long-range electron-transfer defeating the thermal energy trap.

The development of methods to utilize quantum coherence to create new, or to enhance exsting functions in molecular systems represents a grand challenge (*1–4*). Coherent propagation of excitation and charge may enable their directed motion, or ratcheting, over long distances with limited energy loss. A molecular quantum ratchet in principle could take advantage of electronic/vibronic coherences made possible from strongly coupled vibrational modes to move the energy of an absorbed photon from a not-yet-relaxed (nonequilibrium), highly delocalized, initially prepared excited state to a higher energy absorber. The concept of the quantum ratcheted energy transfer has been discussed in the context of natural photosynthetic light harvesting (*5*) and explored further by Hoyer *et al.* (*6*). In such a ratcheted mechanism, an electronically excited chromophore produced by absorption of a low energy photon transports its excitation energy to a neighboring chromophore that would otherwise only absorb photons at a shorter wavelength; harvesting the exciton on the bluer absorber via an ultrafast electron transfer to a linked acceptor locks in the ratcheting. Directed coherent hot exciton migration, coupled to ratcheting, may thus uniquely empower energy conversion reactions, as the transport provides a path to defeat thermalization of the states (e.g., by vibrational cooling and/or internal conversion), enabling kinetic processes that would be forbidden in conventional energy and electron transport theories that assume thermalized initial states. In addition, such a system has the potential to sufficiently expand the coverage of the solar spectrum by the energy conversion device.

Designing molecular quantum ratchet. Here, we describe benchmark experiments that: (i) challenge and test our ability to manipulate coherence in electronically coupled, vibronically mixed multi-chromophore arrays on a time scale shorter than thermalization, and (ii) demonstrate how control of electronic/vibronic coherences can ratchet the energy of non-thermalized excitations to transduce energy. Figure 1 shows a molecular quantum ratchet design D_1D_2A. Our

goal is to engineer a molecular system that facilitates uphill energy flow from donor D_1 to D_2 (uphill in the sense that $\Delta G^{(0)}$ is positive to move from the thermalized D_1* state to the thermalized D_2* state), followed by unidirectional and irreversible electron transfer from the D_2* state to the acceptor ($D_1D_2^+A^-$) state, exploiting vibronic coherence effects to access the $D_1D_2^+A^-$ charge separated state, which is otheriwse inaccessable from the D_1 singlet excited state (D_1*). In order to achieve such successful ratcheting, two conditions must be satisfied: (i) vibronic coupling between D_1 and D_2 should be 'optimal' for unidirectional energy transfer (i.e., the vibronically hot D_1* state should match D_2* states) (*7*) and (ii) D_2* (first singlet excited state of D_2) to A electron transfer must be much faster than the rate of return of the exiton to D_1* and its vibrational relaxation. In our synthetic supramolecular construct, the D_1 unit features a highly conjugated bis[zinc-porphyrin] framework; note that the ethynyl bridge promotes substantial porphyrin-porphyrin electronic coupling and drives globally delocalized ground and excited-states in this supramolecule (*8–11*). In contrast, D_2 in this multichromophoric array is a simple monomeric zinc porphyrin. The lowest energy electronic absorption ($S_0 \rightarrow S_1$) of the D_2 chromophore thus occurs at a shorter wavelength than that for D_1 (Figure 1B). The phenyl ring that links D_1 and D_2 provides only a modest degree of porphyrin-porphyrin electronic coupling (~50 cm^{-1}) (*12*), enabling independent $S_0 \rightarrow S_1$ excitation of D_1 to produce an instantaneously prepared D_1* state in this array. Note that the energy gap between the relaxed D_1* and D_2* is 0.35 eV. Higher lying D_1* vibrational levels thus offer the potential for electronic/vibronic coherences to drive formation of a coherent [D_1-D_2]* electronically excited state (Figure 1A); formation of such a delocalized coherent excited state in this design would also be promoted by the fact that D_1* is characterized by a high oscillator transition moment polarized along its highly conjugated axis. Attached to D_2 is a naphthalene diimide (NDI) electron acceptor (A), defining an excellent platform for ultrafast charge separation

(*13–15*). Note that the direct D_2-A linkage provides electronic coupling more than order of magnitude greater (*15*) than that afforded by the phenyl group that bridges D_1 and D_2. Hence, any D_1 excitation directed to D_2 through electronic/vibronic coherence has the potential to undergo ultrafast adiabatic electron transfer to produce the $D_1D_2^+A^-$ charge separated state on a time scale similar to or faster than the D_1*/D_2 Rabi oscillations that would normally drive relaxation of the coherent [D_1-D_2]* state to D_1*. Because charge delocalization is more extensive in D_1 than in D_2, this design also provides a relaxation pathway for $D_1D_2^+A^-$ to a lower energy $D_1^+D_2A^-$ charge separated state.

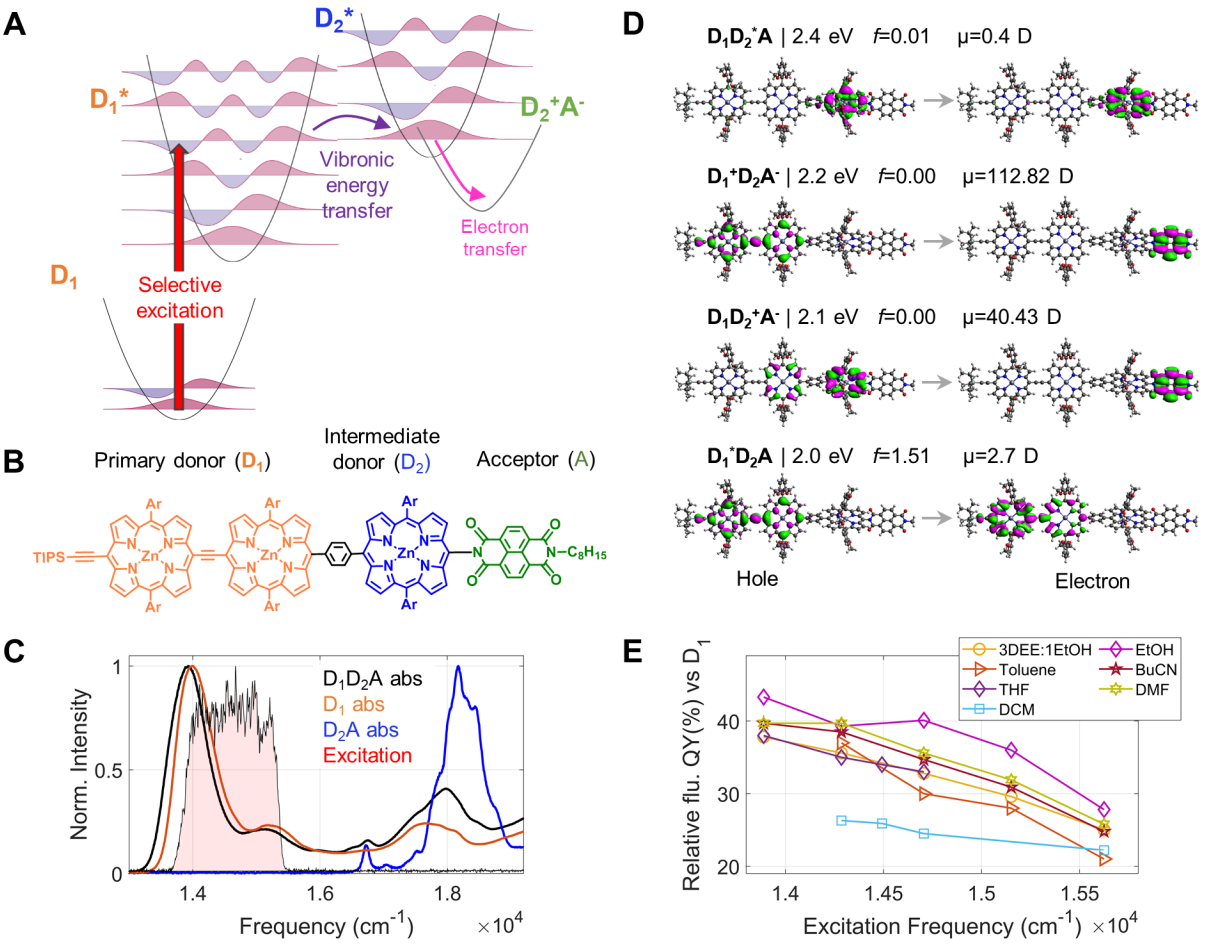

Figure 1. Quantum ratchet and its linear optical properties. (**A**) Schematic representation of vibronic quantum ratcheting. (**B**) Chemical structure of the quantum ratchet molecule. Primary donor (D_1), intermediate donor (D_2) and acceptor (A) units are represented in orange, blue and green respectively. (**C**) Linear absorption spectra of D_1D_2A (black), D_1 (orange) and D_2A (blue) in 3:1 binary solvent mixture of diethyl ether and ethanol at 95K. The excitation spectrum used for transient IR and 2DEV experiments is shown by the filled red curve. (**D**) Molecular orbitals of the excited state transitions enabling ratcheting obtained from TDDFT/TDA analysis. The calculated energies of each excited states, oscillator strength (f) values (indicating the probability of absorbing a photon) and the permanent dipoles (μ) are shown on top. (**E**) Relative (%) fluorescence quantum yield of D_1D_2A compared to D_1 at different excitation frequencies and in different solvents.

Results and Discussion

Excitation frequency dependent fluroscence quenching. A preliminary study of vibronic quantum ratcheting in our D_1D_2A structure was carried out by recording excitation frequency dependent emission of the D_1D_2A construct and D_1 following selective excitation of D_1. A decrease in fluorescence quantum yield in D_1D_2A relative to the parent compound D_1 was observed in both polar and non-polar solvents (Figure 1E). Tuning the excitation frequency to the higher frequency vibronic (100-1500 cm^{-1}) bands of D_1 results in further decrease in the fluorescence quantum yield of D_1D_2A. This indicates that excitation of the D_1 vibronic band in D_1D_2A opens up an additional non-radiative route of excitation relaxation, absent in D_1.

Visible-pump infrared-probe study and evidence of quantum ratcheting. To unravel the decay pathways in D_1D_2A, D_1 unit was selectively excited with a broadband visible pulse centered at 14900 cm^{-1} and a bandwidth of ~1900 cm^{-1}, covering the vibronic shoulder of D_1 (Figure 1C). A mid-infrared pulse over the range 1580-1780 cm^{-1} was used to probe C=O vibrational modes. Among the three building blocks of D_1D_2A, only the NDI acceptor unit (A) contains C=O groups. This provides a unique marker to track the electron transfer by selectively probing the C=O stretching mode of NDI, which shows significant spectral shifts upon formation of the radical anion (*16*, *17*). Figure 2A shows the transient IR spectrum, where ground state bleach (GSB) and photo-induced absorption (PIA) bands are positive (yellow/green) and negative (blue/violet), respectively, in the 2D contour maps. Above 1700 cm^{-1} multiple GSB bands are observed, assigned to the C=O stretching vibrations in the ground electronic state of NDI. Below 1700 cm^{-1} the PIA bands dominate. In particular, within 200 fs after excitation three major PIA peaks are observed at 1628, 1613 and 1596 cm^{-1}. At longer probe delay the GSB bands show monotonic decay, while the PIA bands show an initial rise up to ~70 ps and a decay with a time constant of ~140 ps. A transient IR experiment with resonant (ω_{exc}=17900 cm^{-1}) excitation of D_2A (Figure 2C) shows the same PIA bands at 1596 and 1628 cm^{-1}. However, in contrast to D_1D_2A, the PIA bands show a mono-exponential decay with a time constant of ~90 ps.

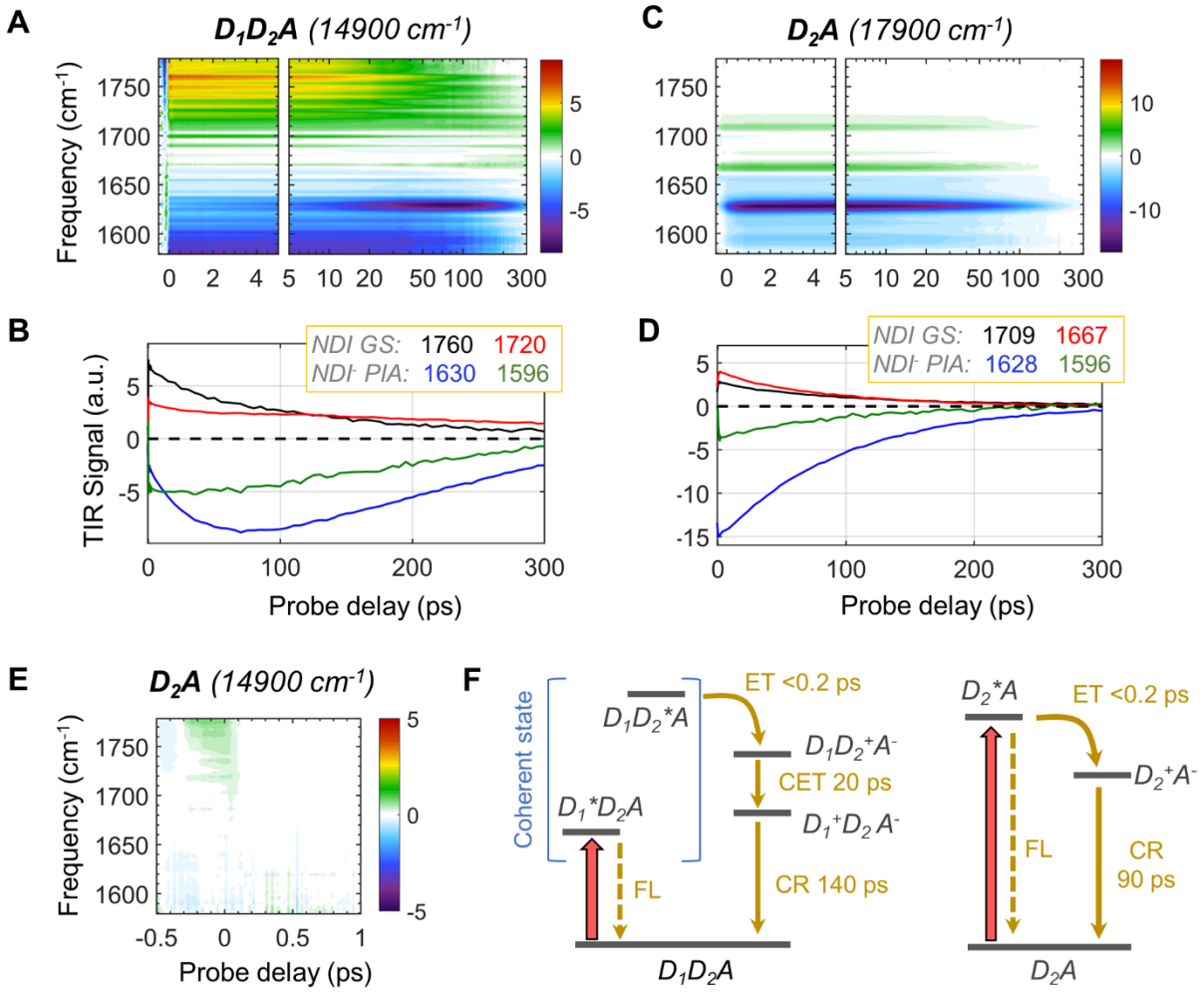

Figure 2. Transient IR spectroscopy. (**A, B**) Spectro-temporal evolution of transient IR signal in D_1D_2A after selective excitation of D_1 with an excitation spectrum centered at 14900 cm^{-1} shown in Figure 1C. (**C, D**) Spectro-temporal evolution of transient IR signal in D_2A after resonant excitation of D_2 with an excitation spectrum centered at 17900 cm^{-1}. In the 2D maps (A and C) probe delay till 5 ps are shown in linear scale while, probe delay from 5 to 300 ps are shown in log-scale. (**E**) Control transient IR experiment with D_2A with same excitation spectrum (ω_{exc}=14900 cm^{-1}) used for D_1D_2A. In each figure positive and negative amplitudes represent ground state bleach (GSB) and photo-induced absorption (PIA) signals, respectively. (**F**) Schematic representation of proposed kinetic model for excitation relaxation in D_1D_2A (left) and

D_2A (right). The thick red arrow represents the excitation and yellow arrows represent different relaxation channels: fluorescence (FL), electron-transfer (ET), cascaded electron-transfer (CET) and charge-recombination (CR).

The IR signatures of the NDI ground state and radical anion are well described in the literature (*16*, *17*). Previous spectrochemical FTIR and transient IR studies on NDI-based compounds have found that the C=O stretching in NDI^- radical anions shows three major characteristic IR peaks at 1630, 1590 and 1514 cm^{-1} (*16*, *17*). Thus, the bands at 1596 and 1630 cm^{-1} in our transient IR spectra are characterized as charge-transfer bands. The appearance of those bands within 200 fs in D_1D_2A indicates rapid formation of the NDI^- radical anion as a result of electron transfer from D_2 to A. Clearly direct excitation of D_2 in D_2A also produces the NDI^- anion, but with entirely different kinetics than upon excitation of D_1 in D_1D_2A. Although our excitation spectrum at 14900 cm^{-1} is not resonant with D_2 (Figure 1C), two-photon absorption could lead to direct excitation of D_2. To ensure that the electron transfer from D_2 to A in D_1D_2A does not arise from direct excitation of D_2 or A via two-photon absorption, we carried out a transient IR control experiment (Figure 2E) with D_2A using the same excitation spectrum (ω_{exc}=14900 cm^{-1}) used for D_1D_2A, and no transient IR signal was found, other than a coherent artifact near time zero due to the overlap of the pump and probe pulses.

The appearance of characteristic charge-transfer bands at 1628 and 1596 cm^{-1} within 200 fs of selective D_1 excitation in D_1D_2A provides *direct evidence of rapid electron transfer* from D_2 to A, which must be the consequence of ratcheted energy transfer from D_1 to D_2. The decay of those charge-transfer bands along, with the GSB bands, indicates relaxation to the ground state

through charge-recombination. In D_2A, charge-recombination happens in ~90 ps. In D_1D_2A, an initial rise of the charge-transfer bands in <70 ps is observed, which suggests conversion of the primary charge-transfer species to an intermediate species before charge-recombination takes place. We propose that the primary charge-transfer species $D_1D_2^+A^-$ forms, through a cascaded electron transfer from D_1 to D_2 (or hole transfer from D_2 to D_1) to generate the intermediate charge-transfer species $D_1^+D_2A^-$, which finally undergoes charge-recombination and relaxation to the ground state. Similar cascaded electron/hole transfer was previously reported for a Pt-based donor-donor-NDI complex (*17*). Our theoretical analysis shows a lower permanent dipole moment for $D_1D_2^+A^-$ (μ= 40.43 D) compared to $D_1^+D_2A^-$ (μ= 112.82 D) (Figure 1D), which in turn, increases the IR transition dipole moment and results in the rise of the transient IR signal. The charge-recombination in $D_1^+D_2A^-$ (~140 ps) is slower compared to the rate in $D_2^+A^-$ (~90 ps), presumably because the charges are spatially more distant in the former case.

Two-dimensional electronic-vibrational spectroscopy. We carried out a two-dimensional electronic-vibrational (2DEV) spectroscopy experiment, which adds a dimension along the excitation frequency axis offering a unique possibility to explore the role of vibronic bands on the ratcheted electron-transfer dynamics. The excitation spectrum used for the 2DEV measurements (Figure 3) on D_1D_2A was the same (ω_{exc}=14900 cm^{-1}) as used for the transient IR experiment. The GSB and PIA bands are represented by red (positive) and blue (negative) colors in each 2DEV map. Although the same IR-peaks are observed across the different excitation frequencies, 2DEV maps show that the relative amplitude of GSB and ESA signals are highly excitation frequency dependent. For example, at T=0.2 ps the GSB bands dominate below ω_{exc}=14200 cm^{-1}, while the PIA bands dominate from 14200 to 15000 cm^{-1} and above 15200 cm^{-1} the relative amplitude of

GSB bands increases. In addition, the 2DEV spectra at all waiting times are structured along the excitation frequency axis. Four dotted lines on Figure 3A, T=0.2 ps represent the maxima of the structured bands, which are separated with an energy gap of about 430-480 cm^{-1}. As the waiting time increases, the 2DEV spectra continue to evolve. While the GSB bands decay, the charge-transfer PIA bands at 1628 and 1596 cm^{-1} initially rise and then decay (Figure 3B), in agreement with our transient IR data (Figure 2B). A closer look at the data indicate that the relative amplitudes of the charge-transfer bands depend on waiting time. In particular, at earlier waiting times (<5 ps), the 1628 cm^{-1} band appears predominantly at the lower excitation frequencies (<14500 cm^{-1}), while at longer waiting times the PIA amplitude spreads across the excitation frequency axis. Furthermore, the excitation frequency dependent dynamics are clearly evident when the 2DEV transients at different excitation frequencies are compared, as shown in Figure 3B. The 1628 cm^{-1} (and 1596 cm^{-1}, shown in SI) PIA band exhibits excitation frequency dependent kinetics; the rise and decay are slower at higher excitation frequencies. In contrast, the decay of the GSB band at 1760 cm^{-1} does not show any significant dependence on the excitation frequency, except at ω_{exc}=14380 cm^{-1}, which seems to show slightly faster kinetics compared to other excitation frequencies and becomes negative at longer probe delay. This might be due to overlap with the negative PIA signal, specially at longer waiting time when the charge-transfer PIA rises in amplitude.

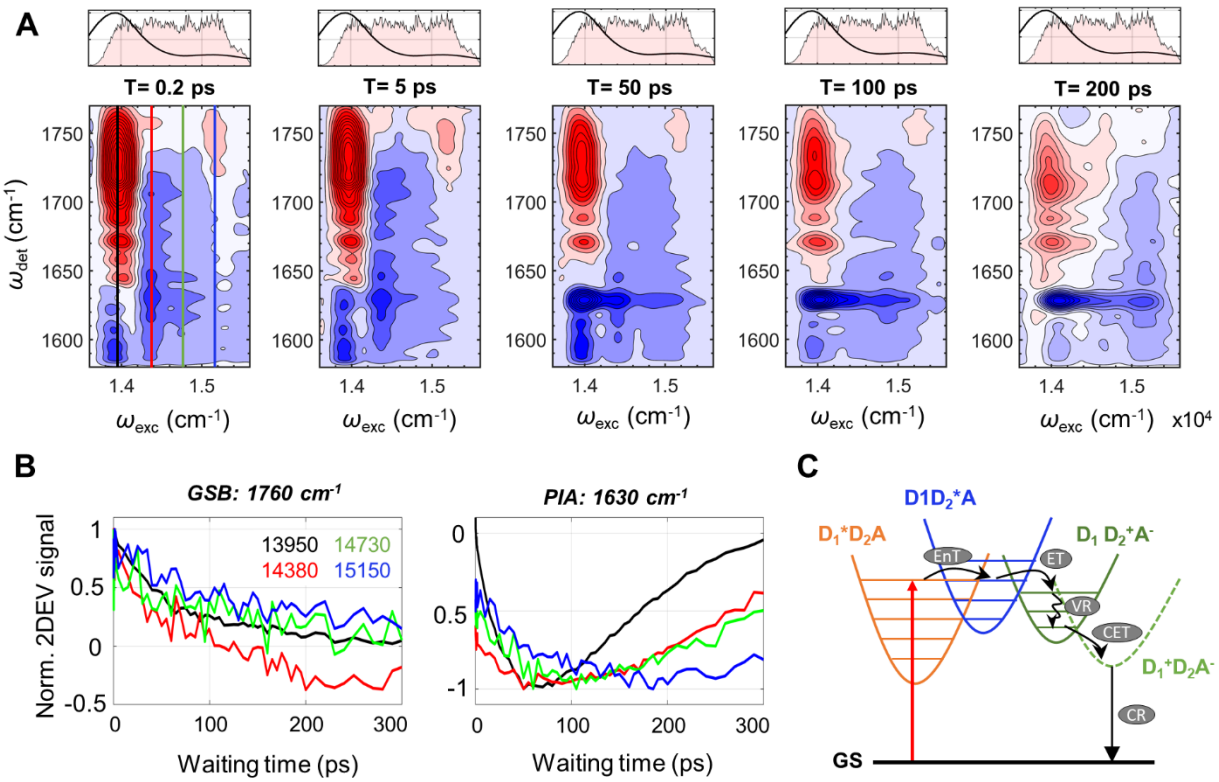

Figure 3. Two-dimensional electronic-vibrational (2DEV) spectroscopy. (**A**) The 2DEV spectra at waiting times T= 0.2, 5, 50, 100 and 200 ps. The normalized linear absorption spectrum (black line) of D_1D_2A and the excitation spectrum (filled red curve) are shown in the top panel. (**B**) The 2DEV transient (each normalized to maximum signal amplitude) of the 1760, 1630 and 1596 IR bands at excitation frequencies 13950 (black), 14380 (red), 14730 (green) and 15150 (blue) cm^{-1}. Those excitation frequencies are marked by vertical lines in 2D map in (A) T=0.2 ps. (**C**) The schematic illustration of population relaxation after excitation of higher vibronic bands of D_1. Different routes of relaxations are represented with arrows: energy transfer (EnT), electron-transfer (ET), cascaded electron-transfer (CET), vibrational relaxation (VR) and charge-recombination (CR).

The higher relative amplitude of the charge-transfer PIA compared to the GSB bands at bluer excitation is consistently observed in the 2DEV, as well as in the transient IR spectra (see SI, Figure S4). In particular, the 2DEV spectrum at >100 ps, when the cascaded electron-transfer is complete, shows that the PIA bands dominate the higher excitation frequency regime. This finding suggests that the excitation of D_1* vibronic band favors the non-radiative charge-transfer route, resulting in higher yield of the final charge-separated species $D_1^+D_2A^-$ compared to the Franck-Condon excitation. This is in line with the excitation frequency dependent fluorescence quantum yield discussed earlier (Figure 1E). Thus, our data suggests involvement of a vibronic coupling between D_1* and D_2* mediating the uphill energy transfer.

The charge-transfer PIA absorption band appears asymmetric along the excitation frequency axis at earlier waiting times, while it gradually spreads out and becomes more even along the excitation axis at longer waiting time (>100 ps). This is a typical signature in 2DEV spectral evolution when population relaxes from higher to lower energy states (*18*, *19*). We assign this as a vibrational cooling process, which typically occurs in a few tens of ps. When the higher vibronic bands of D_1* are excited, the system, after energy transfer from D_1* to D_2* and subsequent electron-transfer from D_2* to A, lands on higher vibrational levels of the $D_1D_2^+A^-$ state that need to undergo vibrational cooling before relaxing to $D_1^+D_2A^-$ (Figure 3C). Hence, the bluer excitation slows down the cascaded electron transfer and subsequent charge-recombination processes, which results in a decrease in the rise and decay rates of the PIA bands at higher excitation frequencies.

Whether specific modes are responsible for the ratcheting effect is not yet clear. This could be addressed by excitation close to the 0-0 band of D_1 followed by a tunable infrared “push” pulse to tune into specific resonance (*20–23*). In addition, specific vibrations could be excited in the ground state as in two-dimensional vibrational-electronic (2DVE) spectroscopy (*24*).

Quantum dynamical simulations. Phenomenological quantum dynamical simulations are in support of the picture described above. The model, described in more detail in the SI (see Figures S2 and S3), includes one explicit vibrational mode (coupled to the D_1* state), and five electronic states (D_1*D_2A, D_1D_2*A, $D_1D_2^+A^-$, $D_1^+D_2A^-$, and the ground state D_1D_2A). The quantum dynamical simulation shows the ratcheting mechanism: the initial exciton is populated in high vibrational states of D_1*, and these excited vibrational levels are in resonance with the lowest vibrational state of D_2*, enabling rapid and coherent exciton delocalization (coherence) assisted by strong excitonic coupling between D_1* and D_2, as well as by the low temperature of the system. Electronic dephasing and vibrational relaxation of the D_1* state, however, decoheres exciton delocalization and eventually localizes the exciton on the D_1* state. However, fast ET from D_2* to A locks in the directional exciton flux to D_2*, defeating return to the D_1* state and thermalization in the D_1* vibronic manifold. Overall, the model predicts rapid population transfer from vibrationally excited D_1*D_2A to D_1D_2*A, which becomes "locked in" by subsequent formation of $D_1D_2^+A^-$ (Figure S2). The model is not intended to quantitatively describe the D_1D_2A system and more precise quantum dynamical calculations will be published elsewhere.

Conclusion

In summary, we demonstrate that strongly coupled arrays of chromophores offer the possibility to use electronic/vibrational coherences in directing the migration of excitation and charge by defeating energy wasting thermalization events. In particular, this study reveals how hot exciton resonance between red and blue absorbers can empower ratcheted charge separation. Such coherent non-equilibrium quantum states enable new paradigms for chemistry that leverage

lossless energy transport, and a subsequent ratcheted ultrafast electron transfer reaction that serves as an irreversible drain, to harvest the energy of non-thermalized excitations. Electronically coupled and vibronically mixed multichromophoric systems not only provide powerful platforms to direct long-range transport with minimal energy loss and expand spectral coverage, but offer new opportunities to tailor control of reactions in which chemistry is liberated from the shackles of Boltzmann statistics.

Methods

Computational methods. Calculations for D_1D_2A (TIPS-PZn2-Ph-PZn-NDI) and subsystems (D_1A, D_2A and D_1D_2) employing Density functional theory (DFT) and Time-Dependent Density Functional Theory with the Tamm-Dancoff approximation (TDDFT/TDA) were performed in Gaussian 16 *(25)* at the MN15/def2-SVP level of theory *(26, 27)*. Aliphatic chains were truncated to methyl groups to reduce the computational cost. Experimental spectra and the CC2 method *(28)* with the same basis set as implemented in TURBOMOLE *(29, 30)* was used to benchmark the chosen DFT functional. Solvation effects were included in DFT and TDDFT/TDA calculations using the polarizable continuum model (PCM) *(31)*. We chose n-pentane (ε=1.83), a solvent with lower dielectric constant than the 3:1 diethyl ether and ethanol mixture, to account for low temperature (95K) and glass sample conditions. Comparable results were obtained with additional implicit solvents (diethylether, toluene).

Visible-pump IR-probe and 2DEV experiment details. A Ti:Sapphire laser based setup has been used for the visible-pump IR-probe and 2DEV measurements. The setup is described elsewhere *(19, 39)*. Briefly, a Ti:Sapphire oscillator (Vitara-S, Coherent) was regeneratively amplified

(Legend, Coherent) with a 1 kHz repetition rate. The amplified pulse was divided into two beams: one beam was used to pump a home-built noncollinear optical parametric amplifier (NOPA); the other beam was used to generate a mid-IR probe pulse (1580 to1780 cm^{-1}) with an optical parametric amplifier-difference frequency generation home-built setup. The NOPA output was compressed to ~16 fs with a prism pair and a pulse shaper (Dazzler, Fastlite). The Dazzler was used to tune the excitation pulse central frequency and bandwidth. The visible pulse was focused on the sample to a spot size of ~250 μm in diameter. The cross-correlation between the visible and mid-IR pulses showed a ~100-120 fs instrument response time. The mid-IR pulse was split by a 50:50 beam splitter to produce a probe and a reference beam. Both IR beams were focused on the sample to a spot size of ~200 μm in diameter. After passing through the sample, the mid-IR beams were dispersed with a spectrometer (Triax 180, Horiba) onto a dual-array 64-pixel HgCdTe detector (Infrared Systems Development). The delay between the visible and IR pulses was controlled by a motorized translation stage.

2DEV has been performed with the same experimental setup, using the Dazzler to generate a pair of visible pulses with relative delay time scanned between 0 and 100 fs with 2.5 fs time steps. Fourier transform has been applied to reconstruct the excitation axis. The visible pulses had central wavelength of 14900 cm^{-1} and a combined energy of ~80 nJ. Because of the pump-probe geometry, a 3 × 1 × 1 phase cycling scheme has been applied to reconstruct the rephasing and non-rephasing signals. All transient IR and 2DEV measurements have been performed at cryogenic temperature (95 K) using an optical cryostat (OptistatDN2, Oxford Instruments). The optical density of the sample at 715 nm was 0.8 with an optical path length of 250 μm. To avoid the photo-bleaching sample spot was changed between each set of measurement.

Data and materials availability: All data are available in the main text or the supplementary materials.

Code Availability: All custom Matlab codes used for experimental data analysis will available on GitHub. The code used in the quantum dynamics simulations will also be released on GitHub.

References and Notes

1. J. L. Brédas, E. H. Sargent, G. D. Scholes, Photovoltaic concepts inspired by coherence effects in photosynthetic systems. *Nat. Mater.* **16**, 35–44 (2016).

2. C. Andrea Rozzi, S. Maria Falke, N. Spallanzani, A. Rubio, E. Molinari, D. Brida, M. Maiuri, G. Cerullo, H. Schramm, J. Christoffers, C. Lienau, Quantum coherence controls the charge separation in a prototypical artificial light-harvesting system. *Nat. Commun.* **4**, 1–7 (2013).

3. G. D. Scholes, G. R. Fleming, L. X. Chen, A. Aspuru-Guzik, A. Buchleitner, D. F. Coker, G. S. Engel, R. Van Grondelle, A. Ishizaki, D. M. Jonas, J. S. Lundeen, J. K. McCusker, S. Mukamel, J. P. Ogilvie, A. Olaya-Castro, M. A. Ratner, F. C. Spano, K. B. Whaley, X. Zhu, Using coherence to enhance function in chemical and biophysical systems. *Nature*. **543**, 647–656 (2017).

4. E. Romero, R. Augulis, V. I. Novoderezhkin, M. Ferretti, J. Thieme, D. Zigmantas, R. Van Grondelle, Quantum coherence in photosynthesis for efficient solar-energy conversion. *Nat. Phys.* **10**, 676–682 (2014).

5. A. Ishizaki, G. R. Fleming, Theoretical examination of quantum coherence in a photosynthetic system at physiological temperature. *Proc. Natl. Acad. Sci. U. S. A.* **106**, 17255–17260 (2009).

6. S. Hoyer, A. Ishizaki, K. B. Whaley, Spatial propagation of excitonic coherence enables ratcheted energy transfer. *Phys. Rev. E - Stat. Nonlinear, Soft Matter Phys.* **86**, 1–14 (2012).

7. P. Bhattacharyya, G. R. Fleming, Quantum Ratcheted Photophysics in Energy Transport. *J. Phys. Chem. Lett.* **11**, 8337–8345 (2020).

8. V. S.-Y. Lin, S. G. DiMagno, M. J. Therien, Highly conjugated, acetylenyl bridged porphyrins: New models for light-harvesting antenna systems. *Science* **264**, 1105–1111 (1994).

9. T. V. Duncan, K. Susumu, L. E. Sinks, M. J. Therien, Exceptional near-infrared fluorescence quantum yields and excited-state absorptivity of highly conjugated porphyrin arrays. *J. Am. Chem. Soc.* **128**, 9000–9001 (2006).

10. J. Rawson, P. J. Angiolillo, M. J. Therien, Extreme electron polaron spatial delocalization in π-conjugated materials. *Proc. Natl. Acad. Sci. U. S. A.* **112**, 13779–13783 (2015).

11. P. P. Roy, S. Kundu, J. Valdiviezo, G. Bullard, J. T. Fletcher, R. Liu, S. J. Yang, P. Zhang, D. N. Beratan, M. J. Therien, N. Makri, G. R. Fleming, Synthetic Control of Exciton Dynamics in Bioinspired Cofacial Porphyrin Dimers. *J. Am. Chem. Soc.* **144**, 6298–6310 (2022).

12. N. P. Redmore, I. V. Rubtsov, M. J. Therien, Synthesis, electronic structure, and electron transfer dynamics of (aryl)ethynyl-bridged donor-acceptor systems. *J. Am. Chem. Soc.* **125**, 8769–8778 (2003).

13. I. V. Rubtsov, N. P. Redmore, R. M. Hochstrasser, M. J. Therien, Interrogating Conformationally Dependent Electron-Transfer Dynamics via Ultrafast Visible Pump/IR Probe Spectroscopy. *J. Am. Chem. Soc.* **126**, 2684–2685 (2004).

14. N. F. Polizzi, M. J. Eibling, J. M. Perez-Aguilar, J. Rawson, C. J. Lanci, H. C. Fry, D. N. Beratan, J. G. Saven, M. J. Therien, Photoinduced Electron Transfer Elicits a Change in the Static Dielectric Constant of a de Novo Designed Protein. *J. Am. Chem. Soc.* **138**, 2130–2133 (2016).

15. N. F. Polizzi, T. Jiang, D. N. Beratan, M. J. Therien, Engineering opposite electronic polarization of singlet and triplet states increases the yield of high-energy photoproducts. *Proc. Natl. Acad. Sci. U. S. A.* **116**, 14465–14470 (2019).

16. I. V. Sazanovich, M. A. H. Alamiry, J. Best, R. D. Bennett, O. V. Bouganov, E. S. Davies, V. P. Grivin, A. J. H. M. Meijer, V. F. Plyusnin, K. L. Ronayne, A. H. Shelton, S. A. Tikhomirov, M. Towrie, J. A. Weinstein, Excited state dynamics of a Pt^{II} diimine complex bearing a naphthalene-diimide electron acceptor. *Inorg. Chem.* **47**, 10432–10445 (2008).

17. A. J. Taylor, E. S. Davies, J. A. Weinstein, I. V. Sazanovich, O. V. Bouganov, S. A. Tikhomirov, M. Towrie, J. McMaster, C. D. Garner, Ultrafast intramolecular charge separation in a donor - Acceptor assembly comprising bis(η^5-cyclopentadienyl)molybdenum Coordinated to an ene-1,2-dithiolate-naphthalenetetracarboxylicdiimide ligand. *Inorg. Chem.* **51**, 13181–13194 (2012).

18. E. A. Arsenault, Y. Yoneda, M. Iwai, K. K. Niyogi, G. R. Fleming, Vibronic mixing enables ultrafast energy flow in light-harvesting complex II. *Nat. Commun.* **11**, 1–8 (2020).

19. E. A. Arsenault, P. Bhattacharyya, Y. Yoneda, G. R. Fleming, Two-dimensional electronic-

vibrational spectroscopy: Exploring the interplay of electrons and nuclei in excited state molecular dynamics. *J. Chem. Phys.* **155**, 020901 (2021).

20. M. Delor, S. A. Archer, T. Keane, A. J. H. M. Meijer, I. V. Sazanovich, G. M. Greetham, M. Towrie, J. A. Weinstein, Directing the path of light-induced electron transfer at a molecular fork using vibrational excitation. *Nat. Chem.* **9**, 1099–1104 (2017).

21. M. Delor, T. Keane, P. A. Scattergood, I. V. Sazanovich, G. M. Greetham, M. Towrie, A. J. H. M. Meijer, J. A. Weinstein, On the mechanism of vibrational control of light-induced charge transfer in donor-bridge-acceptor assemblies. *Nat. Chem.* **7**, 689–695 (2015).

22. M. Delor, P. A. Scattergood, I. V. Sazanovich, A. W. Parker, G. M. Greetham, A. J. H. M. Meijer, M. Towrie, J. A. Weinstein, Toward control of electron transfer in donor-acceptor molecules by bond-specific infrared excitation. *Science* **346**, 1492–1495 (2014).

23. A. A. Bakulin, R. Lovrincic, X. Yu, O. Selig, H. J. Bakker, Y. L. A. Rezus, P. K. Nayak, A. Fonari, V. Coropceanu, J. L. Brédas, D. Cahen, Mode-selective vibrational modulation of charge transport in organic electronic devices. *Nat. Commun.* **6**, 7880 (2015).

24. T. L. Courtney, Z. W. Fox, L. Estergreen, M. Khalil, Measuring coherently coupled intramolecular vibrational and charge-transfer dynamics with two-dimensional vibrational-electronic spectroscopy. *J. Phys. Chem. Lett.* **6**, 1286–1292 (2015).

25. M. J. Frisch, G. W. Trucks, H. B. Schlegel, G. E. Scuseria, M. A. Robb, G. Cheeseman, J. R. Scalmani, V. Barone, G. A. Petersson, H. Nakatsuji, X. Li, M. Caricato, A. V. Marenich, J. Bloino, B. G. Janesko, R. Gomperts, B. Mennucci, H. P. Hratchian, J. V. Ortiz, A. F. Izmaylov, J. L. W. Sonnenberg, F. Ding, F. Lipparini, F. Egidi, J. Goings, B. Peng, A. Petrone, T. Henderson, D. Ranasinghe, V. G. Zakrzewski, J. Gao, N. Rega, G. Zheng, W.

Liang, M. Hada, M. Ehara, K. Toyota, R. Fukuda, J. Hasegawa, M. Ishida, T. Nakajima, Y. Honda, O. Kitao, H. Nakai, T. Vreven, K. Throssell, J. A. Montgomery Jr., J. E. Peralta, F. Ogliaro, M. J. Bearpark, J. J. Heyd, E. N. Brothers, K. N. Kudin, V. N. Staroverov, T. A. Keith, R. Kobayashi, K. Normand, J. Raghavachari, A. P. Rendell, J. C. Burant, S. S. Iyengar, J. Tomasi, M. Cossi, J. M. Millam, M. Klene, C. Adamo, R. Cammi, J. W. Ochterski, R. L. Martin, K. Morokuma, O. Farkas, J. B. Foresman, D. J. Fox, Gaussian 16 Rev. A.03. *Gaussian, Inc.* (2016).

26. H. S. Yu, X. He, S. L. Li, D. G. Truhlar, MN15: A Kohn-Sham global-hybrid exchange-correlation density functional with broad accuracy for multi-reference and single-reference systems and noncovalent interactions. *Chem. Sci.* **7**, 5032–5051 (2016).

27. F. Weigend, R. Ahlrichs, Balanced basis sets of split valence, triple zeta valence and quadruple zeta valence quality for H to Rn: Design and assessment of accuracy. *Phys. Chem. Chem. Phys.* **7**, 3297–3305 (2005).

28. O. Christiansen, H. Koch, P. Jørgensen, The second-order approximate coupled cluster singles and doubles model CC2. *Chem. Phys. Lett.* **243**, 409–418 (1995).

29. TURBOMOLE V7.5.1 2021, A development of University of Karlsruhe and Forschungszentrum Karlsruhe GmbH (2007), , doi:https://www.turbomole.org.

30. S. G. Balasubramani, G. P. Chen, S. Coriani, M. Diedenhofen, M. S. Frank, Y. J. Franzke, F. Furche, R. Grotjahn, M. E. Harding, C. Hättig, A. Hellweg, B. Helmich-Paris, C. Holzer, U. Huniar, M. Kaupp, A. Marefat Khah, S. Karbalaei Khani, T. Müller, F. Mack, B. D. Nguyen, S. M. Parker, E. Perlt, D. Rappoport, K. Reiter, S. Roy, M. Rückert, G. Schmitz, M. Sierka, E. Tapavicza, D. P. Tew, C. Van Wüllen, V. K. Voora, F. Weigend, A.

Wodyński, J. M. Yu, TURBOMOLE: Modular program suite for ab initio quantum-chemical and condensed-matter simulations. *J. Chem. Phys.* **152**, 184107 (2020).

31. G. Scalmani, M. J. Frisch, Continuous surface charge polarizable continuum models of solvation. I. General formalism. *J. Chem. Phys.* **132**, 114110 (2010).

32. C. P. Hsu, Z. Q. You, H. C. Chen, Characterization of the short-range couplings in excitation energy transfer. *J. Phys. Chem. C*. **112**, 1204–1212 (2008).

33. Y. Shao, Z. Gan, E. Epifanovsky, A. T. B. Gilbert, M. Wormit, J. Kussmann, A. W. Lange, A. Behn, J. Deng, X. Feng, D. Ghosh, M. Goldey, P. R. Horn, L. D. Jacobson, I. Kaliman, R. Z. Khaliullin, T. Kuš, A. Landau, J. Liu, E. I. Proynov, Y. M. Rhee, R. M. Richard, M. A. Rohrdanz, R. P. Steele, E. J. Sundstrom, H. L. Woodcock, P. M. Zimmerman, D. Zuev, B. Albrecht, E. Alguire, B. Austin, G. J. O. Beran, Y. A. Bernard, E. Berquist, K. Brandhorst, K. B. Bravaya, S. T. Brown, D. Casanova, C. M. Chang, Y. Chen, S. H. Chien, K. D. Closser, D. L. Crittenden, M. Diedenhofen, R. A. Distasio, H. Do, A. D. Dutoi, R. G. Edgar, S. Fatehi, L. Fusti-Molnar, A. Ghysels, A. Golubeva-Zadorozhnaya, J. Gomes, M. W. D. Hanson-Heine, P. H. P. Harbach, A. W. Hauser, E. G. Hohenstein, Z. C. Holden, T. C. Jagau, H. Ji, B. Kaduk, K. Khistyaev, J. Kim, J. Kim, R. A. King, P. Klunzinger, D. Kosenkov, T. Kowalczyk, C. M. Krauter, K. U. Lao, A. D. Laurent, K. V. Lawler, S. V. Levchenko, C. Y. Lin, F. Liu, E. Livshits, R. C. Lochan, A. Luenser, P. Manohar, S. F. Manzer, S. P. Mao, N. Mardirossian, A. V. Marenich, S. A. Maurer, N. J. Mayhall, E. Neuscamman, C. M. Oana, R. Olivares-Amaya, D. P. Oneill, J. A. Parkhill, T. M. Perrine, R. Peverati, A. Prociuk, D. R. Rehn, E. Rosta, N. J. Russ, S. M. Sharada, S. Sharma, D. W. Small, A. Sodt, T. Stein, D. Stück, Y. C. Su, A. J. W. Thom, T. Tsuchimochi, V. Vanovschi, L. Vogt, O. Vydrov, T. Wang, M. A. Watson, J. Wenzel, A. White, C. F. Williams, J. Yang,

S. Yeganeh, S. R. Yost, Z. Q. You, I. Y. Zhang, X. Zhang, Y. Zhao, B. R. Brooks, G. K. L. Chan, D. M. Chipman, C. J. Cramer, W. A. Goddard, M. S. Gordon, W. J. Hehre, A. Klamt, H. F. Schaefer, M. W. Schmidt, C. D. Sherrill, D. G. Truhlar, A. Warshel, X. Xu, A. Aspuru-Guzik, R. Baer, A. T. Bell, N. A. Besley, J. Da Chai, A. Dreuw, B. D. Dunietz, T. R. Furlani, S. R. Gwaltney, C. P. Hsu, Y. Jung, J. Kong, D. S. Lambrecht, W. Liang, C. Ochsenfeld, V. A. Rassolov, L. V. Slipchenko, J. E. Subotnik, T. Van Voorhis, J. M. Herbert, A. I. Krylov, P. M. W. Gill, M. Head-Gordon, Advances in molecular quantum chemistry contained in the Q-Chem 4 program package. *Mol. Phys.* **113**, 184–215 (2015).

34. R. J. Cave, M. D. Newton, Generalization of the Mulliken-Hush treatment for the calculation of electron transfer matrix elements. *Chem. Phys. Lett.* **249**, 15–19 (1996).

35. H. P. Breuer, F. Petruccione, *The Theory of Open Quantum Systems* (Oxford University Press, USA, 2002).

36. G. Lindblad, On the generators of quantum dynamical semigroups. *Commun. Math. Phys.* **48**, 119–130 (1976).

37. S. Akimoto, T. Yamazaki, I. Yamazaki, A. Osuka, Excitation relaxation of zinc and free-base porphyrin probed by femtosecond fluorescence spectroscopy. *Chem. Phys. Lett.* **309**, 177–182 (1999).

38. H. S. Eom, S. C. Jeoung, D. Kim, J.-H. Ha, Y.-R. Kim, Ultrafast Vibrational Relaxation and Ligand Photodissociation / Photoassociation Processes of. *J. Phys. Chem. A*. **101**, 3661–3669 (1997).

39. T. A. A. Oliver, N. H. C. Lewis, G. R. Fleming, Correlating the motion of electrons and nuclei with two-dimensional electronic-vibrational spectroscopy. *Proc. Natl. Acad. Sci.*

U. S. A. **111**, 10061–10066 (2014).

Acknowledgments: The authors acknowledge the Center for Synthesizing Quantum Coherence, supported by the National Science Foundation (CHE-1925690), for funding this research. P. P. R, C. L. and G. R. F. thank the U.S. Department of Energy, Office of Science, Chemical Sciences, Geosciences, and Biosciences Division for research and equipment support. Z.X.W.W., J.V., and S.C. acknowledge CHE-1925690, and R.L., PZ., J.P.M., D.N.B., and M.J.T. thank CHE-2109020 for research support. JV thanks the National Science Foundation under Grant # 2127309 for support to the Computing Research Association for the CIFellows 2021 Project.

Author contributions:

Conceptualization: MJT, GRF

Methodology: MJT, DNB, GRF

Investigation: PPR, ZXWW, CL, JV, RL, PZ, JPM, SC

Funding acquisition: DNB, MJT, GRF

Supervision: GRF, MJT, DNB

Writing – original draft: PPR, GRF, MJT, DNB, JV, ZXWW

Writing – review & editing: PPR, GRF, MJT, DNB, JV, ZXWW, PZ, CL, SC, RL, JPM

Competing interests: Authors declare that they have no competing interests.

Supplementary Materials

Supplementary Text

Figs. S1 to S4

Tables S1

Supporting Information

Light-driven electron transfer by Quantum vibronic ratcheting

Partha Pratim Roy[1,2], Zachary X. W. Widel[3], Rui Liu[3], Jesús Valdiviezo[1,3,4,8], Peng Zhang[3], Cristina Leonardo[1,2], Jarrett P. Mansergh[3], Sutirtha Chowdhury[3], David N. Beratan[3,5,6], Michael J. Therien[3] and Graham R. Fleming[1,2,7]*

Affiliations:

[1]Department of Chemistry, University of California, Berkeley, CA 94720, USA.

[2]Molecular Biophysics and Integrated Bioimaging Division, Lawrence Berkeley National Laboratory, Berkeley, CA 94720, USA.

[3]Department of Chemistry, Duke University, Durham, North Carolina 27708, United States.

[4]Department of Electrical and Computer Engineering, Duke University, Durham, North Carolina 27708, United States.

[5]Department of Physics, Duke University, Durham, North Carolina 27708, United States.

[6]Department of Biochemistry, Duke University, Durham, North Carolina 27710, United States.

[7]Kavli Energy Nanoscience Institute at Berkeley, Berkeley, CA 94720, USA.

[8]Kenneth S. Pitzer Center for Theoretical Chemistry, Berkeley, CA 94720, USA.

*Corresponding author. Email: grfleming@lbl.gov

Calculations of electronic couplings

Energy transfer (EET) couplings were calculated employing the Fragment Excitation Difference (FED) method *(32)* as implemented in Q-Chem 5.3.2 *(33)*. Electron transfer (ET) couplings between initial (i) and final (f) excited states (V_{if}) were calculated using the generalized Mulliken-Hush (GMH) method *(34)*. Dipole moments and energy differences were obtained from TDDFT/TDA calculations.

The electronic structure and photophysical properties of the compound were studied using density functional theory (DFT) and time-Dependent Density Functional Theory with the Tamm-Dancoff approximation (TDDFT/TDA). Calculated absorption spectra of D_1D_2A demonstrate qualitative agreement between calculations and experiments (Figure S1). Computed TDDFT/TDA analysis of the locally excited ($D_1^*D_2A$ and $D_1D_2^*A$) and charge-transfer ($D_1D_2^+A^-$ and $D_1^+D_2^+A^-$) excited states of the D_1D_2A system in implicit n-pentane solvent are shown in Figure 1D. Energetics of excited states (Figure 1D) show energy level ordering required for quantum ratcheting dynamical simulation.

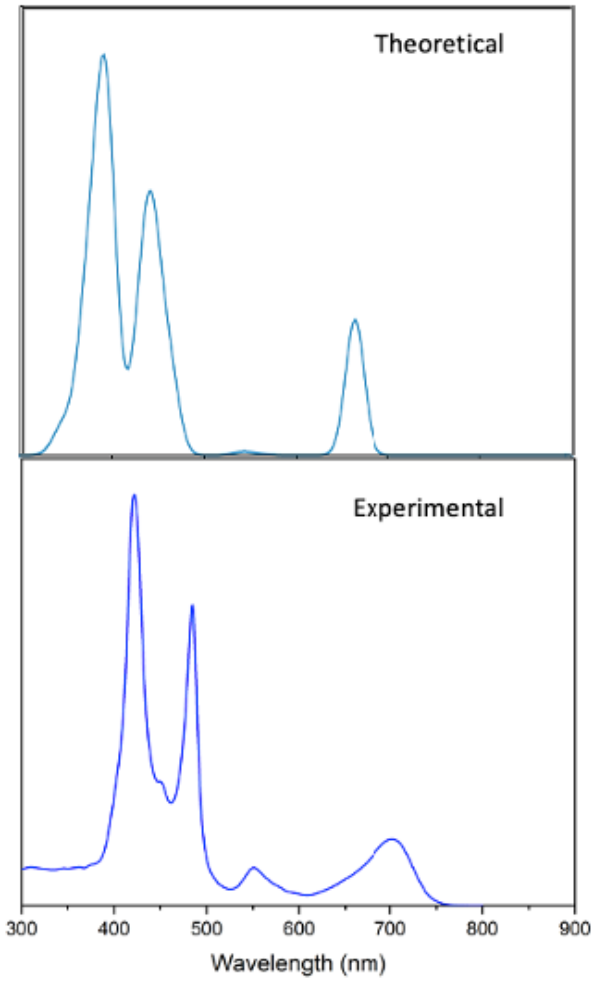

Fig. S1. Theoretical and experimental absorption spectra of D_1D_2A in diethylether. The theoretical spectrum was obtained from a TDDFT/TDA analysis at the MN15/def2-SVP level of theory.

Table S1 shows the eletronic couplings (V) calculated using the Fragment Excitation Difference (FED) Method for EET and Generalized Mulliken Hush (GMH) method for ET. A strong EET electronic coupling between $D_1{*}D_2A$ and $D_1D_2{*}A$ enables initial energy transfer, followed by electron transfer between $D_1D_2{*}A$ and $D_1D_2^{+}A^{-}$. Later, the $D_1D_2^{+}A^{-}$ forms.

Table S1. Calculated electronic couplings. Eletronic couplings (V) calculated at the Franck-Condon geometry using the Fragment Excitation Difference (FED) Method for EET and Generalized Mulliken Hush (GMH) method for ET.

Initial state	Final state	V/eV	Type
D_1*D_2A	D_1D_2*A	1.08E-02	EET
D_1D_2*A	$D_1D_2^+A^-$	3.98E-05	ET
$D_1D_2^+A^-$	$D_1^+D_2A^-$	1.74E-02	ET
$D_1^+D_2A^-$	D_1*D_2A	1.01E-04	ET

Quantum dynamical simulations using Lindblad master equation

Phenomenological quantum dynamical simulations were preformed to show how the four key excited electronic states evolve in time, and to indicate the physical origins of electron transfer based ratcheting. In this simplified quantum model of the excited state dynamics, the system Hamiltonian (H_s) includes one explicit vibrational mode (coupled to the D_1* state), and five electronic states (D_1*D_2A, D_1D_2*A, $D_1D_2^+A^-$, $D_1^+D_2A^-$, and the ground state D_1D_2A).

$$H_S = \sum_I (h_I + \varepsilon_I)|I\rangle\langle I| + \sum_{I \neq J} V_{IJ}|I\rangle\langle J|,$$

The five electronic states are indexed with the subscript I, and V_{IJ} is the state-to-state electronic coupling, and e_I is the energy of electronic state I. The nuclear motion is harmonic, and is written using the mass weight coordinate Q:

$$h_I = \frac{P^2}{2} + \frac{1}{2}\omega^2(Q - Q_I)^2.$$

Here P is the momentum, Q_I is the coordinate shift of the electronic state I, and w is the vibrational frequency. The Huang-Rhys factor is related to the reorganization energy $\lambda = S\hbar\omega$.

In the simulation, we further assume that there are N vibrational levels on D_1*D_2A, and only one vibrational level is considered on all other electronic states. The energy of the N^{th} vibrational level on D_1*D_2A is in resonance with the D_1D_2*A vibrational level. A schematic representation of this system Hamiltonian is shown in Figure S2 below. The relative energies (e_I) of the electronic states are parameterized based on quantum chemical computations (see Fig. S2). We assume that the vibrational frequency is w = 300 cm^{-1}, and N = 7 (i.e., there are seven vibronic levels). The Huang-Rhys factor S between the two exciton states D_1*D_2A and D_1D_2*A is set to 3.17 and for all other pair states S=1, for simplicity.

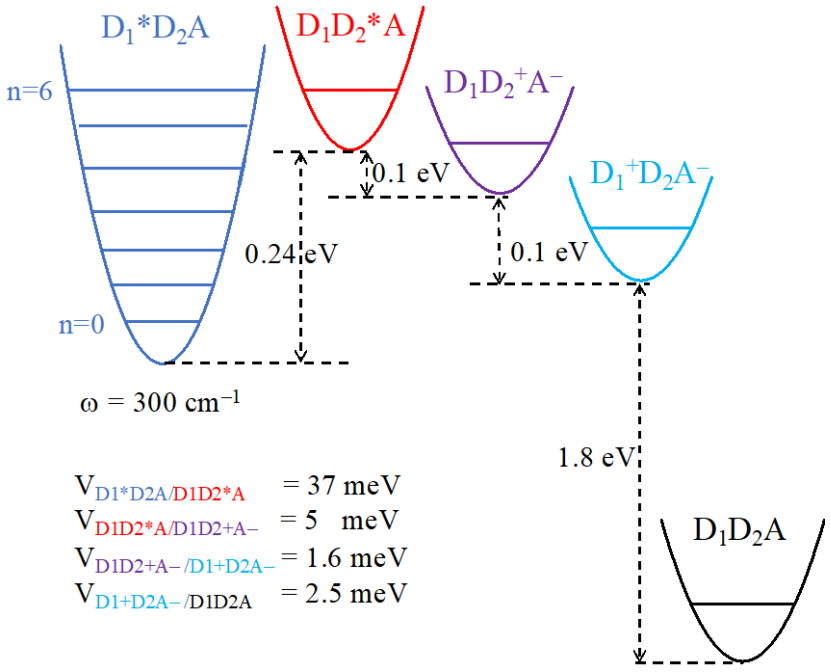

Fig. S2. Schematics representation of the potential energy profiles for the coupled electron and exciton transfer in the D_1D_2A ratchet. The electronic couplings and energetics indicated are used in the quantum dynamical simulations. The coupling values are chosen in this illustrative dynamical simulation to represent the qualitative features of the population evolution found experimentally.

We model the dissipative dynamics using the Lindblad approach *(35, 36)*. The time evolution of the system density matrix is given by

$$\frac{d}{dt}\rho(t) = \frac{1}{i\hbar}[H_s, \rho(t)] + \sum_{mn}\left\{L_{mn}\rho(t)L_{mn}^{\dagger} - \tfrac{1}{2}\left[L_{mn}^{\dagger}L_{mn}\rho(t) + \rho(t)L_{mn}^{\dagger}L_{mn}\right]\right\}.$$

Here L_{mn} is a set of operators describing the dissipative dynamics. In the simulations, we consider electronic pure dephasing and vibrational relaxation. For pure dephasing,

$$L_{mn} = \delta_{mn}\sqrt{\gamma_m}|m\rangle\langle m|,$$

where $|m\rangle$ is the electronic state and γ_m is the dephasing rate. Since the pure dephasing operators are diagonal, the populations $\rho_{mm}(t)$ remain unchanged as the system evolves. This implies that energy is conserved during the evolution, as the bath cannot drain energy from the system. However, the coherences described by the off-diagonal density matrix elements, $\rho_{mn}(t)$, decay exponentially with a rate given by $\tau_{mn} = (\gamma_m + \gamma_n)$. For the vibrational relaxation, the Lindblad operator is off-diagonal,

$$L_{mn} = (1 - \delta_{mn})\sqrt{\gamma_{mn}}|m\rangle\langle n|.$$

$|m\rangle$ refers to the vibrational state and γ_{mn} is the vibrational transition rate. The downward and upward transition rates are related by $\gamma_{mn} = e^{\hbar\omega/k_BT}\gamma_{nm}$, ensuring that the populations of the equilibrium states obey detailed balance. We further assume that vibrational relaxation occurs only

between nearest neighbor vibronic levels, $n = m \pm 1$. Since the experiment was carried out at 95K, we choose a relatively slow dephasing rate. The exciton pure dephasing rate is 1/100 fs^{-1}, and the dephasing rate for electron transfer is 1/50 fs^{-1}. The downward vibrational relaxation rate is 1 ps^{-1}, a typical value for porphyrin like systems *(37, 38)*.

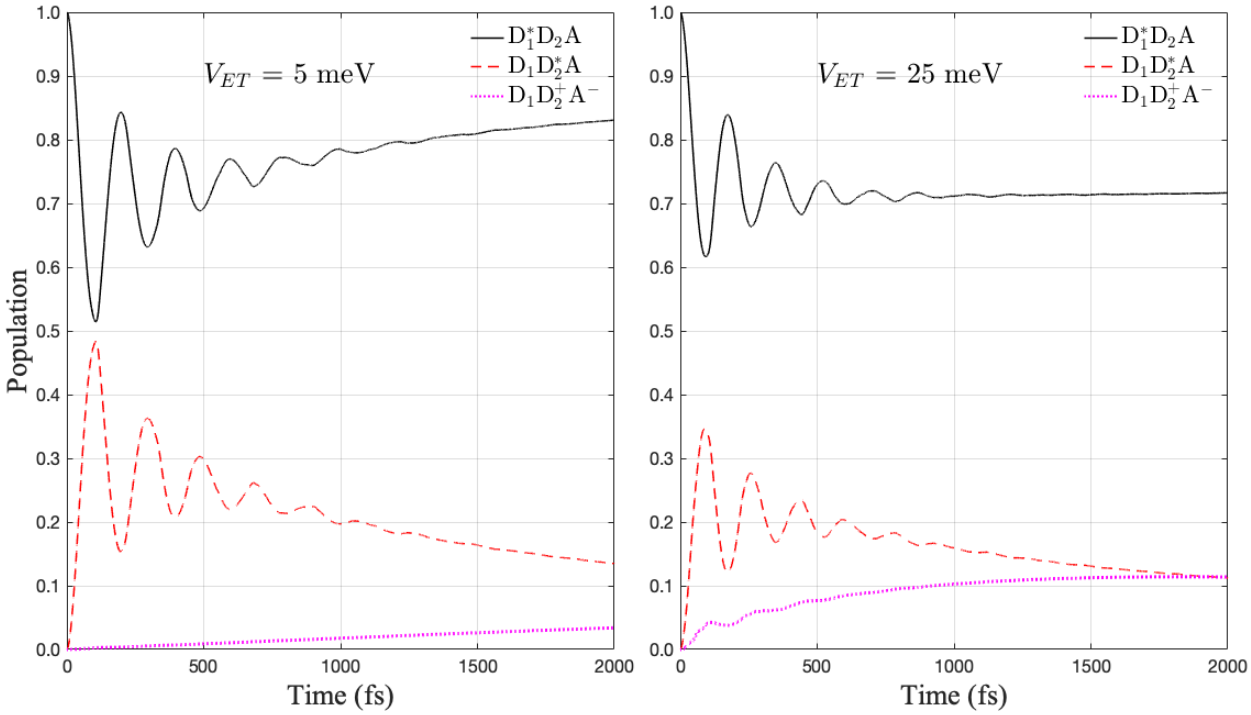

Fig. S3. Quantum dynamical simulations for electron transfer ratcheted coherent exciton transfer. The time evolving populations of the two exciton states (D_1*D_2A and D_1D_2*A) and the charge separated state ($D_1D_2^+A^-$) are computed (left and right panels, respectively) using two different D_2*A/$D_2^+A^-$ ET coupling strengths (V_{ET}).

Excitation frequency dependent transient IR experiments

The transient IR experiments were carried out with two different excitation spectrum, 14500 and 15000 cm^{-1} (Figure S4). Both show a very similar transient spectral appearance and

evolution with increase in pump-probe delay. However, a stark difference in relative amplitude of ground state bleach and photo-induced absorption bands. The excitation of higher-frequency D_1* vibronic bands increases the relative amplitude of PIA compared to GSB suggesting that D_1* vibronic excitation facilitates non-radiative electron-transfer route, which is agreement with our excitation-frequency dependent fluorescence study (Figure 1E) as well as 2DEV study (Figure 3A). Furthermore, the rise and decay of PIA bands become slower with higher excitation while, the decay of GSB bands remain unaffected. This is again in agreement with our 2DEV results discussed in the main text (Figure 3B).

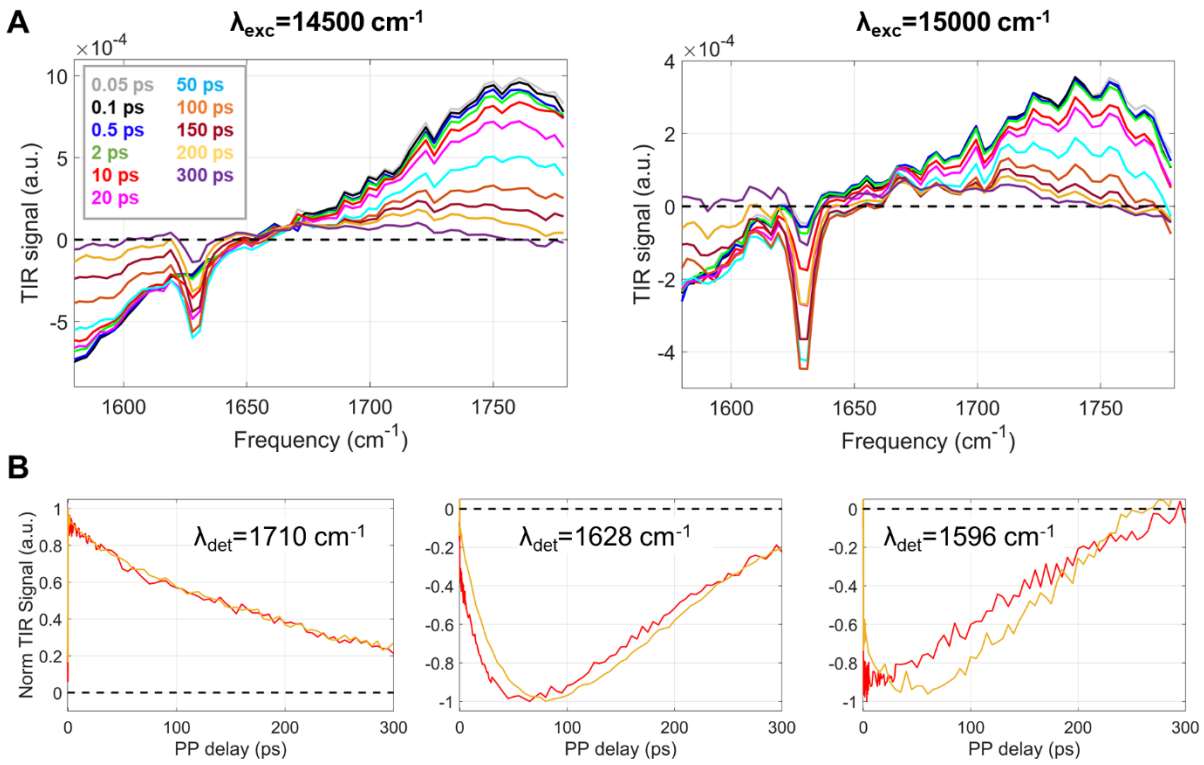

Fig. S4. Excitation frequency dependent transient IR. (A) The evolution transient IR spectra with increase in pump-probe delays with the excitation spectrum centered at 14500 cm^{-1} (left) and 15000 cm^{-1} (right). (B) The transients at three different detection frequencies: 1710, 1628 and 1596

cm^{-1}. The red and yellow colors in each graph represent the transient IR experiments obtained with excitation spectrum centered at 14500 and 15000 cm^{-1}, respectively.